

REPORT DOCUMENTATION PAGE				Form Approved OMB No. 0704-0188	
Public reporting burden for this collection of information is estimated to average 1 hour per response, including the time for reviewing instructions, searching existing data sources, gathering and maintaining the data needed, and completing and reviewing this collection of information. Send comments regarding this burden estimate or any other aspect of this collection of information, including suggestions for reducing this burden to Department of Defense, Washington Headquarters Services, Directorate for Information Operations and Reports (0704-0188), 1215 Jefferson Davis Highway, Suite 1204, Arlington, VA 22202-4302. Respondents should be aware that notwithstanding any other provision of law, no person shall be subject to any penalty for failing to comply with a collection of information if it does not display a currently valid OMB control number. PLEASE DO NOT RETURN YOUR FORM TO THE ABOVE ADDRESS.					
1. REPORT DATE (DD-MM-YYYY) 24-03-2015		2. REPORT TYPE Final		3. DATES COVERED (From - To)	
4. TITLE AND SUBTITLE Extraordinary TCR in Carbon nanotube-polymer composites and device implications in bolometric infrared detection				5a. CONTRACT NUMBER	
				5b. GRANT NUMBER W911NF-12-2-0069	
				5c. PROGRAM ELEMENT NUMBER	
6. AUTHOR(S) Jimmy Xu, Gustavo E Fernandes, Jin Ho Kim, Patrick Tae, Chong Zhao.				5d. PROJECT NUMBER	
				5e. TASK NUMBER	
				5f. WORK UNIT NUMBER	
7. PERFORMING ORGANIZATION NAME(S) AND ADDRESS(ES) Brown University 182 Hope Street Providence, RI 02912, USA				8. PERFORMING ORGANIZATION REPORT NUMBER	
9. SPONSORING / MONITORING AGENCY NAME(S) AND ADDRESS(ES) US Army Research Laboratory, RDRL-SER-L 2800 Powder Mill Road, Adelphi, MD 20783, USA				10. SPONSOR/MONITOR'S ACRONYM(S)	
				11. SPONSOR/MONITOR'S REPORT NUMBER(S)	
12. DISTRIBUTION / AVAILABILITY STATEMENT Approved for public release; distribution is unlimited.					
13. SUPPLEMENTARY NOTES					
14. ABSTRACT The development of high TCR materials, such as vanadium oxide (VOx), has enabled the introduction of bolometric infrared sensors to the field of uncooled infrared imagers and detection. Many other devices are currently available for remote thermometry applications (i.e. laser thermometer "guns") and small pixel-count thermal cameras are beginning to make their way into the realm of consumer electronics, although their cost/performance ratio still is unsatisfactory. We propose a study of a new material platform that holds the promise of both breaking the current record of TCR achieved in VOx and introducing a new threshold-activation responsivity. This new material, made of polymer-carbon nanotube composite, is inherently low in mass density, high in broadband absorption, flexible and conformal, and scalable in size. We shall also investigate the feasibility of tuning the peak TCR value and the threshold temperature via compositional and polymer engineering. With an order of magnitude increase in TCR over that of VOx achievable in this new platform, this study could lead to a substantial improvement in bolometric IR responsivity and a potential breakthrough in IR response speed, and thereby to a novel, scalable, high speed and high sensitivity base material for deployment in future bolometric IR detectors.					
15. SUBJECT TERMS Bolometers, infrared sensing, detectors, focal plane array.					
16. SECURITY CLASSIFICATION OF:			17. LIMITATION OF ABSTRACT	18. NUMBER OF PAGES	19a. NAME OF RESPONSIBLE PERSON
a. REPORT Unclassified	b. ABSTRACT Unclassified	c. THIS PAGE Unclassified	UU	31	19b. TELEPHONE NUMBER (include area code)

20150415184

Final Report (1 copy)

Defense Technical Information Center (DTIC)

8725 John J. Kingman Road, Suite 0944

Ft. Belvoir, VA 22060-6218

**Extraordinary TCR in Carbon nanotube-polymer composites and device
implications in bolometric infrared detection
(W911NF-12-2-0069)**

Jimmy Xu

Professor of Engineering and Professor of Physics

Brown University, Providence, RI 02912

Jimmy_Xu@Brown.edu

ARL-Technical point of contact:

Dr. Madan Dubey

US Army Research Laboratory,

Sensors and Electron Devices Directorate, RDRL-SER-L,

2800 Powder Mill Road,

Adelphi, MD 20783

V:301-394-1186

madan.dubey@us.army.mil

Foreword

This final technical report contains three main sections describing researches that were undertaken within the scope of this project. In the first section we describe carbon nanotube membrane microbolometers, operating uncooled in the near-IR and mid-IR bands, with high speed (10 ms) and high responsivity (kV/W). The microbolometers were fabricated in a vertical process on a thin suspended silicon nitride film for thermal isolation. The measured effective time-constant was 10 ms, and the detectivity was $\sim 5.5 \times 10^6 \text{ cmHz}^{1/2}\text{W}^{-1}$ at 40 Hz. We find that the broadband spectral responses measured at room temperature over the entire band of the IR illumination source are characteristic of bolometric response. These results are indicative of the potential of this platform for high-speed uncooled IR sensing and thermal imaging in a focal plane array format. The measured device noise indicated a relatively strong $1/f$ contribution though, which is common of CNT devices operated in atmospheric conditions.

In the second section we report on uncooled mid-infrared photovoltaic responses arising in heterojunction diodes of reduced graphene oxide with p-Si. This study was initially motivated by “broken devices” produced in the experiment described above, where occasional shorts between the silicon substrate and the CNT membranes led to photovoltaic responses in the infrared. Two major photoresponse spectral peaks are observed, one in the near infrared starting at $1.1 \mu\text{m}$ corresponding to electron-hole pair generation in the Si substrate, and another for wavelengths below $2.5 \mu\text{m}$, arising from properties of the reduced graphene oxide-Si contact. Our analysis of the current-voltage characteristics at various temperatures suggest that the two materials form a type-II (broken-gap) heterojunction, with a characteristic transition between direct tunneling to field emission, to over-the-barrier excitation with increasing reverse voltage. Illumination was found to affect the onset of the transition between direct tunneling and field-emission, suggesting that the mid infrared response results from the excitation of minority carriers (electrons) from the Si and their collection in the reduced graphene oxide contact. The photoresponse near $1.1 \mu\text{m}$ showed a time constant at least five times faster than the one at $2.5 \mu\text{m}$, which points to surface defects as well as high series resistance and capacitance as potentially limiting factors in this mode of operation. With proper device engineering considerations, these devices could be promising as a platform for infrared sensing. Similar responses were also recorded with devices made with CNT films instead of reduced graphene oxide, but the responses from reduced graphene were larger.

Finally, in the third section we investigate the material properties of and in particular the temperature coefficient of resistance (TCR), of carbon nanotube composites with the phase-change polymer Poly(N-isopropylacrylamide) (PNIPAm). Our results shed light on the underlying mechanism of electron transport through networks of conductive paths in the composites and its dependence on the molecular

weights of the phase-changing polymer. Measurements of the humidity dependence of the TCR and reveal the dominant conduction mechanism to be variable range hopping with an exponent of $1/4$, corresponding to transport in a 3D system. In a humid atmosphere, a twenty-fold change in the hopping activation energy is observed as the temperature is swept across the polymer's hydrophilic-to-hydrophobic phase-transition, while no change is observed in low humidity atmospheres or in vacuum. The TCR was found to depend on molecular weight but to also be affected by details of the dynamics of hydration/dehydration of the composites. For operation in dry atmospheres and in vacuum the maximum TCR observed was only .002%, while in a humid atmosphere the TCR as large as 60% were observed- an order of magnitude higher than those found in common high-TCR materials used in thermal sensing applications.

Each of the sections described here have been written into manuscripts. The first section has already been published in Applied Physics Letters, and the third section has been reviewed by IOP Nanotechnology and is awaiting final decision. The second section is in the final stages of preparation for submission.

Table of Contents

Title	1
Foreword	2
Table of Contents	4
Statement of the Problem Studied	5
Summary of the most important results	5
- High speed, high responsivity, uncooled carbon nanotube microbolometers	5
- Reduced Graphene Oxide Mid-Infrared Photodetector at 300K	13
- Molecular weight effects on the phase-change-enhanced temperature coefficient of resistance in carbon nanotube/ Poly(N-isopropylacrylamide) composites	21
Bibliography	31

Statement of the problem studied

The development of high TCR materials, such as vanadium oxide (VOx), has enabled the introduction of bolometric infrared sensors to the field of uncooled infrared imagers and detection. Many other devices are currently available for remote thermometry applications (i.e. laser thermometer “guns”) and small pixel-count thermal cameras are beginning to make their way into the realm of consumer electronics, although their cost/performance ratio still is unsatisfactory. We propose a study of a new material platform that holds the promise of both breaking the current record of TCR achieved in VOx and introducing a new threshold-activation responsivity. This new material, made of polymer-carbon nanotube composite, is inherently low in mass density, high in broadband absorption, flexible and conformal, and scalable in size. We shall also investigate the feasibility of tuning the peak TCR value and the threshold temperature via compositional and polymer engineering. With an order of magnitude increase in TCR over that of VOx achievable in this new platform, this study could lead to a substantial improvement in bolometric IR responsivity and a potential breakthrough in IR response speed, and thereby to a novel, scalable, high speed and high sensitivity base material for deployment in future bolometric IR detectors.

Summary of the most important results

I - High speed, high responsivity, uncooled carbon nanotube microbolometers

** This section was published in Applied Physics Letters, Appl. Phys. Lett. 104, 201115 (2014).*

I.1 – Introduction

Uncooled infrared (IR) detectors have become indispensable in a number of military, emergency, and safety applications, allowing for the ability to navigate in zero illumination and in vision-obscured environments, such as smoke or fog. Since their development in the 1970's, uncooled IR detectors have branched out from their military origins and have provided great advantages to soldiers on the battlefield, search-and-rescue crews, and night-time drivers, with their ability to peer into the IR wavelength range of typically 8-12 μm . Originally pursued in order to reduce the cost, weight, and reliability issues compared with cryogenically cooled thermal imagers, multiple uncooled thermal imaging technologies were explored, including ferroelectrics/pyroelectrics, thermopiles, and microbolometers.¹ Amongst them, microbolometers have stood out as the technology of choice for uncooled thermal imaging due to the benefits of their faster operating frequencies, their ability to achieve superior sensitivity due to higher noise

equivalent temperature difference (NETD), their reduced need for thermoelectric temperature stabilization, and their ability to integrate into Si CMOS electronics for integration into existing processes.

With about 30 years of development, vanadium oxide-based microbolometers have become the current standard for uncooled IR detectors, but bolometers based on amorphous silicon (α -Si) have also become common since their introduction in the 1990's.^{1,2} These materials act as thermistors, with a thermal coefficient of resistivity (TCR) between 1-3%. Carbon nanotubes (CNTs) have recently been studied as an alternative material to VOx and α -Si with a reported TCR of less than ~1%.^{3,4} Commonly observed responsivity are in the neighborhood of a few hundred V/W with time constants ranging from 5-100 ms.^{3,4}

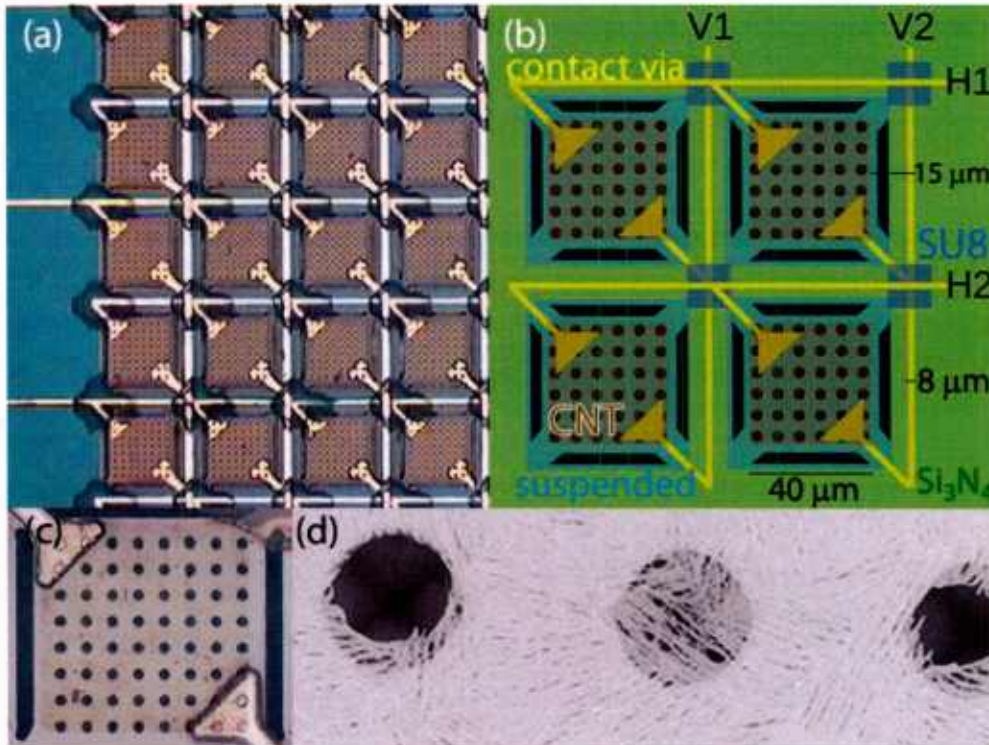


FIGURE 1. CNT microbolometers. (a) Portion of an 8-by-8 microbolometer array with multiplexed contacts. The dark patches are SU8 insulating pads, and each pixel is 40 μm by 40 μm . (b) Schematic of sample. H1,2 and V1,2 indicate horizontal and vertical vias for multiplexing. (c) Close-up view of a single pixel showing suspended silicon nitride structure with CNT film atop with contact pads. CNT film appears slightly darker on the image. (d) Scanning electron micrograph of CNT film stretched over some of the holes on the silicon nitride membrane. The holes are 3 μm in diameter.

In this work, we designed and developed a vertical layer-by-layer fabrication approach that uses silicon nitride (Si_3N_4) coated silicon wafers as substrates. The Si_3N_4 layer served to both electrically isolate the pixels from the Si substrate, as well as to enable the suspension of the thin CNT membrane over the silicon substrate and form suspended microbolometer pixels anchored on the corners. The suspension improves thermal isolation of the pixels, which is necessary for achieving high bolometric responsivity. For the proof-of-concept demonstration, we targeted an 8-by-8 array of suspended and contacted pixels. Here, we report on the spectral photoresponse, responsivity and detectivity of single pixels measured at room-temperature in ambient pressure and without cooling or temperature regulation. For comparison, measurements were also recorded with illumination through a silicon filter, which removed the visible component of the illumination and any responses originating from the device's silicon substrate. A Ge filter, with a cut-off at 0.66 eV, which is well below the silicon bandgap (1.12 eV), was also used. We measured the broadband photoresponses in these devices that are characteristically bolometric with a time constant of $\sim 10\text{ms}$ and a broadband spectral response covering the entire IR range of the illumination source and optics used in the Fourier-transform infrared spectrometer (FTIR). As such, the platform shows potential for high-speed, uncooled infrared detectors for various applications.

I.2 – Experiment

CNT Pixel Array Fabrication

We used a vertical-layering process based on a substrate consisting of 100 nm Si_3N_4 deposited onto a p-type Si substrate ($\langle 100 \rangle$, 10 Ohm-cm) via a plasma-enhanced chemical vapor deposition (PE-CVD) process - the Si_3N_4 coated wafers were purchased from University Wafers. The process begins with the definition of windows on the Si_3N_4 layer via positive tone photolithography (Shipley 1818 resist, Karl-Suss mask aligner), followed by the reactive ion etching (RIE) of the Si_3N_4 (100 W, $\text{CF}_4 - 38\text{ sccm}$, $\text{O}_2 - 2\text{ sccm}$, 50 mTorr). The windows permit the subsequent wet-etching of the Si underneath the Si_3N_4 structures to obtain suspended Si_3N_4 membranes that will serve as support for the CNT pixels. Following the patterning of the windows onto Si_3N_4 , additional photolithography processes are used to deposit (Ti/Pd) metal contacts with terminals at each pixel. A vertical-horizontal multiplex scheme is used in the contact layout, which requires two layers of contacts with insulation pads between crossing contact vias. The first layer of contacts is defined via positive tone photolithography (S1818) followed by the deposition of 5 nm Ti and 50-100 nm Pd, which is then followed by lift off in acetone. After the first layer of contacts is deposited, a set of insulating pads are patterned using the SU-8 negative tone resist (SU-8 2002). The SU-8 resist provides chemically resistant and robust insulating pads between the vertical and horizontal vias. The second set of contacts is then deposited following the same process as the first.

With contacts in place, a CNT-film is then transferred to the substrate. The process begins with a solution of water-dispersed, single-walled CNTs consisting of a 67:33 mixture of semiconducting and metallic tubes, respectively. To form CNT films with high uniformity, the solution is vacuum filtered through a porous polymer-membrane filter with a mean pore diameter of $\sim 20\text{nm}$. The polymer filters pads with a CNT film layer atop are then placed onto the substrate face down, with the CNT film in direct contact with the substrate. The polymer film is then dissolved with acetone, transferring the CNT film to the substrate. The chip with the CNT film attached is then soaked in acetone followed by ethanol, and dried under a stream of nitrogen gas. It was observed that the CNT film adheres very well to the smooth silicon nitride film surface. The transferred CNT film is then patterned into squares with dimensions $40\text{ }\mu\text{m}$ by $40\text{ }\mu\text{m}$ aligned with the Si_3N_4 windows. Finally, the sample is subjected to a 0.2 Mol/L KOH bath at $80\text{ }^\circ\text{C}$ for approximately 2 hours. This step etches the Si underneath the Si_3N_4 windows, leaving suspended Si_3N_4 membranes with contacted CNT films atop. Figure 1 shows microscope images and a schematic diagram of the device.

Characterization

The samples were mounted onto a copper block to provide heat sinking, with contacts made with micromanipulator tips directly to breakout pads that address individual pixels. For broadband measurements, illumination was accomplished through the probe-station microscope, which is equipped with a halogen-tungsten lamp illuminator. A mechanical chopper modulated the light and enabled lock-in detection. The individual pixels were biased in constant voltage mode through a voltage divider circuit obtained by placing a load-resistor ($20\text{ k}\Omega$, 1%) in series with the pixel. The load-resistor was chosen to have resistance similar to the pixel. The changes in voltage drop across the pixel were measured directly with a lock-in amplifier (SR830, Stanford Research Inc.). The input impedance of the lock-in amplifier ($10\text{ M}\Omega$) is considerably greater than the resistance of a pixel. I-V curves were also recorded for each pixel using a semiconductor parameter analyzer (Agilent 4155B, Agilent Inc.) to check that they were Ohmic. Noise measurements were performed using a spectrum analyzer (SR760, Stanford Research Inc.). Spectral photoresponse measurements were performed using a FTIR system (Bruker Equinox 55) equipped with a tungsten-halogen illumination source and quartz beam splitter. Step-scan mode was used with phase modulation at 22 Hz . The sample was biased at 1.5 V and the current amplified by a current-to-voltage converter prior to being fed into the FTIR spectrometer's external detector port. The current-to-voltage amplifier gain was adjusted as needed between the measurements.

I.3 – Results and Discussion

The photoresponse and responsivity of the devices in bolometric mode are shown in Figure 2. The bias across the pixel and load-resistor was 3V, which corresponded to less than 100 μ A flowing across each pixel. Much smaller currents (~ 10 uA) were also tested and gave consist results. Different illumination conditions were used, including broadband illumination with a tungsten-halogen lamp at power densities of 1.7 and 14 mW/cm² with and without a Si filter, which removed the visible component of illumination. The photoresponse was also recorded with point source illumination achieved by shining a collimated diode laser (~ 1 mW) directly through the microscope eyepiece, which formed a uniform laser spot $\sim 5 \mu\text{m}^2$ in the field of view. The laser spot was placed directly at the center of the pixel for the measurement labeled as “laser spot” in Figure 2. Tests were also performed with the laser spot onto neighboring pixels, which caused the photoresponse to vanish ascertaining that the photoresponses observed were localized to a single pixel, without significant pixel-to-pixel crosstalk.

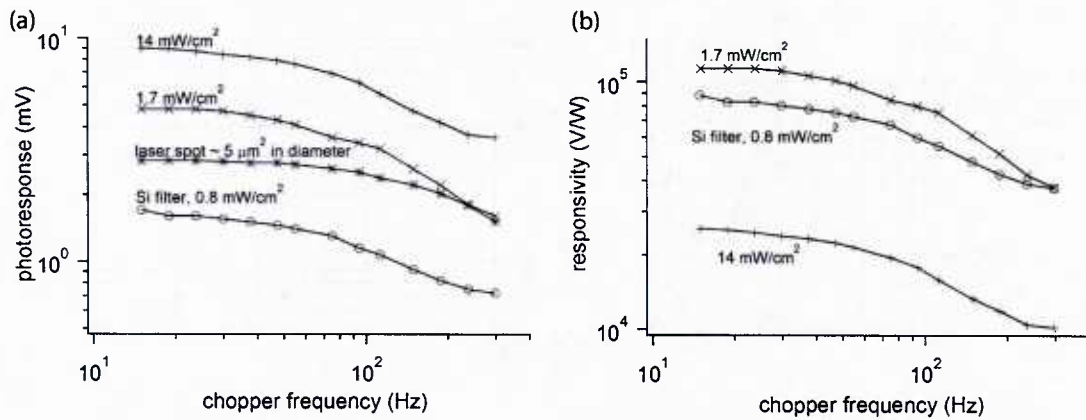


FIGURE 2. Bolometric photoresponse (a) and responsivity (b) of CNT pixel for various conditions of illumination power density, as indicated in the labels. Part (a) includes a photoresponse measurement done with a laser focused to a small spot ($\sim 5 \mu\text{m}$) onto one pixel under test to confirm that the observed response originated from the pixel instead of neighboring structures. The label “Si filter” indicates measurements taken with the illumination filtered by a double-side polished Si wafer with resistivity 100 Ohm-cm.

The photoresponses observed were characteristically bolometric and decreased with increasing modulation frequency. The -3 dB point in this mode of photoresponse was observed to occur at a modulation frequency of ~ 100 Hz. The corresponding responsivity curves are shown in Figure 2 (b). The pixels showed better performance at smaller illumination power densities ($\sim 1.7 \text{ mW/cm}^2$) than at larger power densities ($\sim 14 \text{ mW/cm}^2$). We attribute this to substrate heating at the large illumination power density. It is worthwhile noting that the responsivity with the Si filter in place was comparable to that with

full broadband illumination, which eliminates the possibility of the responses measured here being due to electron-hole pair creation in the Si substrate. If electron-hole pair creation in the Si substrate played a significant role in the responses observed, we would expect the Si filter to cause the responsivity to decrease by several orders of magnitude.⁵ A Ge filter was also used in the spectral photoresponse measurements described below, and also showed consistent results.

To further characterize these devices, we measured the bandwidth normalized noise voltage (V_n) and calculated the resulting detectivity $D^* = \Re \sqrt{A} / V_n$, where \Re is the responsivity (V/W) and A is the effective pixel area (cm²), as shown in Figure 3. The pixel noise voltages, shown in Figure 3 (a) are relatively large and show a 1/f trend. Both of these features are typical of CNT devices in open-package and at ambient pressure.⁶ The load resistance noise voltage was measured by replacing the pixel with another resistor (identical to the load) in the voltage divider network. It was then subtracted in quadrature from the measurement taken with the pixel in the network to obtain the pixel noise voltage. The noise due to the load resistor, which is also representative of the system noise, is seen to be ~ 2 orders of magnitude smaller than the pixel noise. The detectivity, Figure 3 (b), was found to be $\sim 1 \times 10^7$ cm Hz^{1/2} W⁻¹ at 100 Hz, which is in agreement with other reported values.^{3,7}

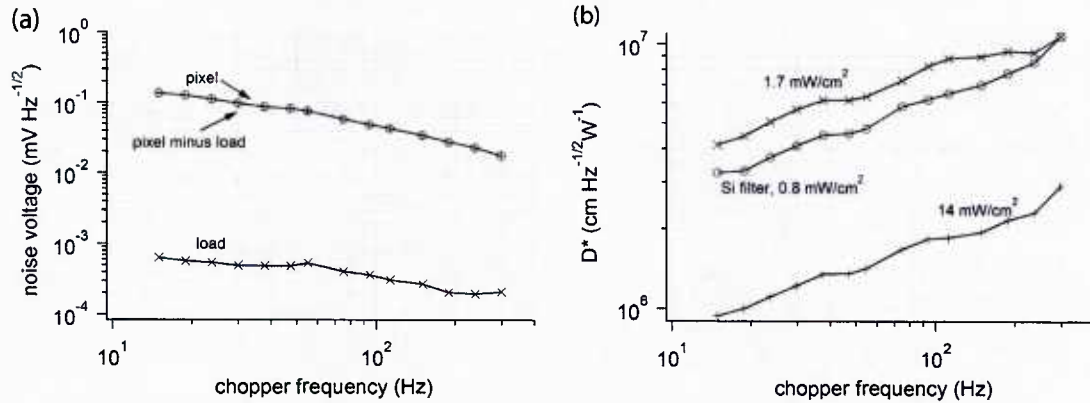


FIGURE 3. Noise voltage (a) and detectivity (b) of a CNT bolometer pixel. The detectivity is plotted for various conditions of bias and illumination power, following the symbol convention in Figure 2.

Figure 4 shows the spectral photoresponse of these devices measured with a FTIR spectrometer in step-scan mode. The devices showed broadband photoresponse spanning the entire source spectral range, which can be seen by comparing with the source spectrum collected with the spectrometer's built-in DLaTGS detector, shown in Figure 4(d). Normalization was not performed so as to preserve the regions of smaller signal at the edges of the spectrum, as numerical noise makes the data in these regions less clear when normalization to the source intensity is performed.

The broadband photoresponse observed is characteristic of a bolometric action as well as the broadband absorption of carbon nanotubes. No device optimizations for enhancing the absorption efficiency of these devices were performed. Optimizations, such as incorporation of structural or material provisions including quarter wave spacing between the suspended membrane and the substrate for constructive interference, as well as addition of IR absorbing materials onto the pixels could enhance the performance of these devices. Pixel dimensions were chosen arbitrarily for this study, with limitations being imposed by the available optical lithography setup. Because operation at room temperature and pressure conditions were chosen for this study, the question may arise as to whether the ~ 10 ms time constant obtained is dominated by oxygen desorption/adsorption. We believe, however, that this was not a significant factor in these devices. Collins et al ⁸ have reported on the effects of oxygen adsorption as resulting in an increase in the hole concentration, leading to increased conductivity. Such mechanism would thus result in an increase in the pixel resistance upon illumination, mimicking the behavior of a positive TCR device. The photoresponses observed in these devices were, however, consistent with a negative TCR.

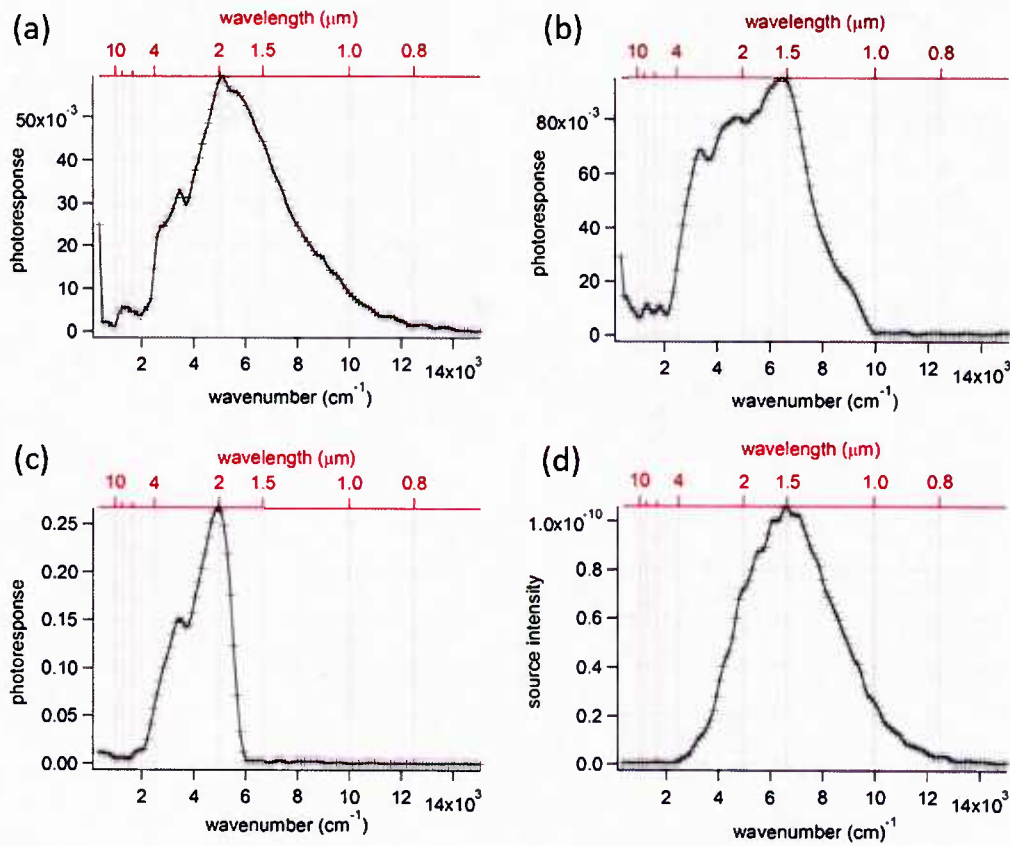


FIGURE 4. Photoresponse spectra of (a) pixel, (b) pixel with Si filter, (c) pixel with Ge filter, and (d) IR source spectrum collected with the FTIR spectrometer's built-in DLaTGS detector for comparison. The y-axes are in arbitrary units.

I.4 – Conclusion

We demonstrated carbon nanotube microbolometer focal plane arrays with pixels suspended on a Si_3N_4 membrane. The figures of merit, namely the time constant, detectivity, and responsivity measured in this proof-of-concept device are favorable, with fast 10 ms response time at the lower end as compared with other studies on CNT bolometers and comparable with that observed in the vanadium oxide and α -Si platforms. The detectivity also compares favorably with other reports on CNT bolometers to date, and is affected by the inherently large $1/f$ noise observed in CNT systems. The measured temporal and broadband spectral responses suggest that these detectors are operating in the bolometric mode. The performance parameters observed here are encouraging for application in uncooled IR sensing and imaging.

I.5 – References

- ¹ Antoni Rogalski, *Infrared detectors*, 2nd ed. (Taylor & Francis, Boca Raton, 2011), pp.xxi.
- ² Paul W. Kruse, *Uncooled thermal imaging : arrays, systems, and applications*. (SPIE Press, Bellingham, Wash., USA, 2001), pp.xviii.
- ³ A. E. Aliev, *Infrared Phys. Technol.* **51** (6), 541 (2008); M. E. Itkis, F. Borondics, A. P. Yu, and R. C. Haddon, *Science* **312** (5772), 413 (2006); R. T. Lu, Z. Z. Li, G. W. Xu, and J. Z. Wu, *Appl. Phys. Lett.* **94** (16), 163110 (2009); P. Merel, J. B. A. Kpetsu, C. Koechlin, S. Maine, R. Haidar, J. L. Pelouard, A. Sarkissian, M. I. Ionescu, X. L. Sun, P. Laou, and S. Paradis, *Comptes Rendus Physique* **11** (5-6), 375 (2010).
- ⁴ G. E. Fernandes, J. H. Kim, A. K. Sood, and J. Xu, *Adv. Funct. Mater.* **23** (37), 4678 (2013).
- ⁵ C. A. Mead, *Solid State Electron* **9** (11-1), 1023 (1966).
- ⁶ E. S. Snow, J. P. Novak, M. D. Lay, and F. K. Perkins, *Appl. Phys. Lett.* **85** (18), 4172 (2004).
- ⁷ Alexander Y. Glamazda, Victor A. Karachevtsev, William B. Euler, and Igor A. Levitsky, *Adv. Funct. Mater.* **22** (10), 2177 (2012); M. B. Jakubinek, M. A. White, M. F. Mu, and K. I. Winey, *Appl. Phys. Lett.* **96** (8), 083105 (2010); R. T. Lu, J. J. Shi, F. J. Baca, and J. Z. Wu, *J. Appl. Phys.* **108** (8), 084305 (2010); R. T. Lu, G. W. Xu, and J. Z. Wu, *Appl. Phys. Lett.* **93** (21), 213101 (2008); M. Tarasov, J. Svensson, L. Kuzmin, and E. E. B. Campbell, *Appl. Phys. Lett.* **90** (16), 163503 (2007).

II - Reduced Graphene Oxide Mid-Infrared Photodetector at 300K

**This section is in the final preparation stages and will be submitted to Applied Physics Letters shortly*

II.1 – Introduction

Contacts between reduced graphene oxide (rGO) and other materials, primarily Si, are potentially fruitful platforms for infrared detection – as an alternative to pristine graphene, rGO presents benefit of allowing broader tuning of its optical and electronic properties via both chemical (i.e. reduction and oxidation) and physical processes. The optical band-gap of rGO is tunable over a large spectral range,¹ covering the mid and near infrared spectral ranges as well as a significant portion of the visible. Si is a natural substrate material for rGO because, besides its already established role in electronics and photonics, contacts between Si and various carbonaceous materials have shown room temperature photovoltaic responses in the near to mid-infrared ranges.^{2,3} For carbon species having a band-gap, the commonly proposed infrared photoresponse mechanism involves the direct photo-generation of excitons in the carbon-based electrode followed by their dissociation by the built-in fields at the heterojunction with Si, with carrier collection occurring at the metal electrodes. For carbon species without a band gap, the mechanism of photogeneration appears to be consistent with photo-assisted emission in a Schottky contact.^{3,4}

Recent studies on graphene-Si photodetectors have targeted telecom applications focusing on high responsivity and high bandwidth within the 1450-1590 nm wavelength range. Responsivity in excess of 100 mA/W with bandwidth of 20 GHz have been demonstrated in waveguide-coupled graphene-Si devices,^{4,5} which were also shown to be compatible with CMOS processing⁶ facilitating device. In such graphene-Si devices, direct photo-excitations between the graphene Dirac points comprise an important component of the observed photoresponse.⁴ A recent report has also identified the role of indirect (phonon assisted) transitions in graphene, yielding additional photoresponses in the mid infrared (2.75 μm).⁴ Photoresponses at longer wavelength have also been demonstrated, but appear to rely on different mechanisms, such as coupling between plasmons in the graphene and phonons in an underlying SiO₂ layer.⁷ Reports of graphene photodetectors not involving Si have also demonstrated mid infrared responses with high responsivity but low bandwidth,⁸ suggesting that thermal effects (bolometric and Seebeck) dominated the photoresponse.

In the case of rGO-Si devices, interband photo-transitions as well as surface charge accumulation at the interface may be important factors in determining photoresponses. Oxygen-based defects have been found to dramatically improve the near infrared response of metal-rGO-metal devices.⁹ Enhanced

absorption effects arising from properties of the rGO structure, such as electron-phonon coupling enabled by oxygen aggregations at defects¹⁰ and defect-driven infrared absorption.¹¹ Works on metal-rGO-metal photoconductive/bolometric devices have found generally large responsivity but also very long time constants, again suggesting bolometric or thermovoltaic (Seebeck) effects as dominant mechanisms.¹² Zhu et al¹³ have reported on rGO/n-Si devices for operation in the visible and demonstrated that control of reduction and annealing conditions can dramatically affect both the photoresponse linearity and time constant. A recent work on hybrid rGO/ZnO nanostructure photodetectors¹⁴ has reported high responsivity in the visible range. While infrared responses in rGO devices are at present somewhat underexplored, other studies have reported on other applications of rGO-Si structures, including electronic diodes,^{15,16} batteries¹⁷ and photochemical devices.¹⁸

In this letter, we report on mid-infrared photoresponses in rGO/p-Si heterojunction diodes in uncooled mode and operating at room temperature. These diodes show a photoresponse band in the near infrared (at 1.1 μm) corresponding to electron-hole pair generation in the Si substrate, and another for wavelengths below 2.5 μm , arising from excitation of minority carriers from the Si into the rGO. We find that these diodes show voltage-dependent transport mechanisms in the reverse bias region, and that only the high voltage reverse bias regime is strongly affected by illumination, which also causes the onset voltage of field emission transport mode to change. Our measurements of the temperature and voltage dependence of the reverse current and reconstruction of the device energy-band diagram suggests a type-II (broken-gap) heterojunction structure. The observed device characteristics suggest that rGO-Si contacts could offer a promising platform for infrared sensing applications. The advent of tunable band gap in rGO as well as potentially large variations in the work function depending on synthesis parameters open the possibility for realizing a host of interesting heterojunction structures, some of which may be particularly suited for mid infrared sensing.

II.2 – Experiment

An aqueous solution of rGO was produced according to the procedure described elsewhere. The solution was vacuum filtered through a polypropylene porous membrane filter with mean pore diameter of 20 nm to yield highly uniform rGO films. A 1.5 cm X 1.5 cm clean p-type Si chip (0.005 ohm-m) was half-covered by a 25 μm thick SU-8 2025 film in order to create an isolated region for contacting the rGO film. After SU-8 film deposition the substrate was submerged in a 5% HF solution for 15 minutes to remove the native oxide. The rGO film was then transferred to the prepared Si substrate immediately after HF treatment so as to make contact with the both the exposed Si and the SU-8 surface. For electrical contacts, a small area on the back of the Si wafer was scratched with a diamond scribe and a thin copper wire was soldered to it with indium. Silver paste was used on the rGO side making sure that the contacting region occurred only on the

area of the rGO film located above the SU-8 mesa so as to avoid creating silver paste shorts to the silicon substrate. A schematic of the obtained device is shown in Figure 1(b). The final rGO-Si contact area was $\sim 0.8\text{cm} \times 0.8\text{cm}$. For photoresponse measurement, the device was connected to a transimpedance amplifier (P-9202-5, Gigahertz Optik), the output of which went to the external detector port of a Fourier transform infrared (FTIR) spectrometer (Equinox 55, Bruker). Reverse bias of 0.8V was used in the measurements. The spectrometer was operated in step-scan mode with phase modulation. Illumination was provided by a Globar source at a power density of 8.5 mW/cm^2 and a KBr beamsplitter was used. The FTIR spectrometer was also used to measure the absorbance of the rGO. For this purpose an identical rGO film to the one used in the device was deposited on a double side polished high resistivity Si window – the absorbance was calculated from transmission and reflection measurements. Additional I-V tests were performed with a source measure unit (Keithley, 236). Vacuum measurements were performed in a closed cycle He cryostat (DE-202, APD Cryogenics) and the temperature was adjusted with an external computer-controlled unit (9620-I, Scientific Instruments Inc.). Thickness measurements for the rGO films were performed using an atomic force microscope (MFP-3D, Asylum Research).

II.3 – Results and discussion

Figure 1 (a) shows the observed photoresponses measured at different phase modulation frequencies. The prominent peak starting at 9000 cm^{-1} corresponds to photogenerated e-h pairs in the Si substrate, which are separated by the heterojunction built-in potential and collected at the rGO and In contacts. This type of near infrared photoresponse is well-known in Si heterojunction devices.¹⁹ Of particular interest to us is the also prominent peak occurring below $\sim 5000\text{ cm}^{-1}$, which corresponds to mid-infrared photoresponses in the device. Analysis of the peak intensity variation with phase modulation frequency (Figure 1(b)) reveals that the mid infrared photoresponse has a -3db cutoff time constant of 25ms - 5 times larger than the photoresponse in the Si substrate. Measurements performed with a Ge filter in front of the device (cutoff at $\sim 5330\text{ cm}^{-1}$, not shown) also confirm that the two photoresponse peaks are independent of each other and not a result of spectral folding. The mid infrared responsivity was approximately 2.7 mA/W at 11 Hz modulation. The responsivity due to the Si substrate (i.e. near infrared) was not measured but is seen to be several orders of magnitude larger than the mid infrared responsivity by comparing the relative intensities of the global source. We note that the spectra in Figure 1(a) are not normalized to the Globar intensity because such normalization would introduce significant numerical noise in the near infrared data.

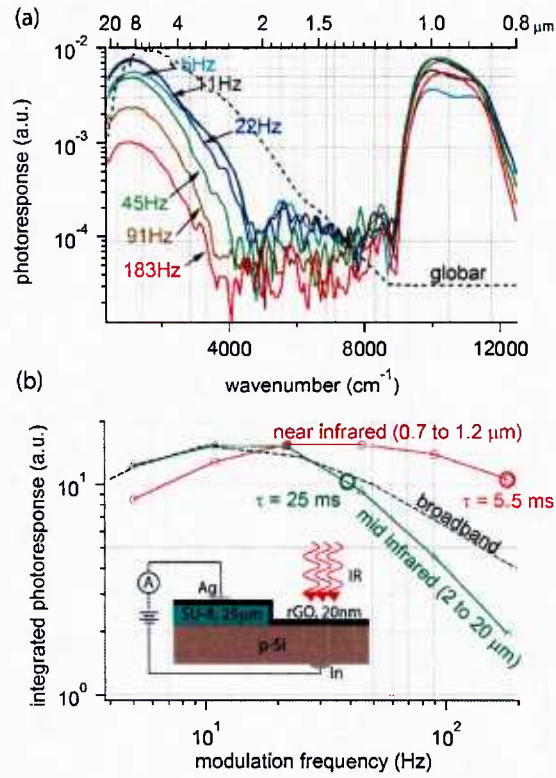


FIGURE 1. (a) Normalized spectral photoresponse at various modulation frequencies. The dashed line in (a) shows the globar spectrum as measured by the FTIR spectrometer's deuterated triglycine sulfate (DTGS) detector and rescaled. (b) Near infrared, mid infrared, and broadband photoresponses as a function of modulation frequency. Inset shows device schematic.

Figure 2 (a) shows the I-V characteristic of the device with and without illumination (from a broadband tungsten-halogen lamp $\sim 3\text{mW}/\text{cm}^2$). Voltage is applied to the rGO side of the device and the shape of the I-V characteristic suggests that the forward direction corresponds to negative voltage on the rGO side/positive voltage on the Si side. Diode behavior is observed in the I-V characteristic, with a large reverse leakage current. Illumination is seen to affect only the high voltage reverse bias portion of the I-V characteristic. In particular the low voltage ($<1\text{V}$) portion of the I-V characteristic is almost unaffected by illumination. We note that the change in I-V characteristic due to broadband illumination is primarily a result of e-h pair generation in Si. Mid infrared photoresponse measurements were also repeated at zero bias (short-circuit mode) but yielded much lower responsivity than the reverse bias measurement.

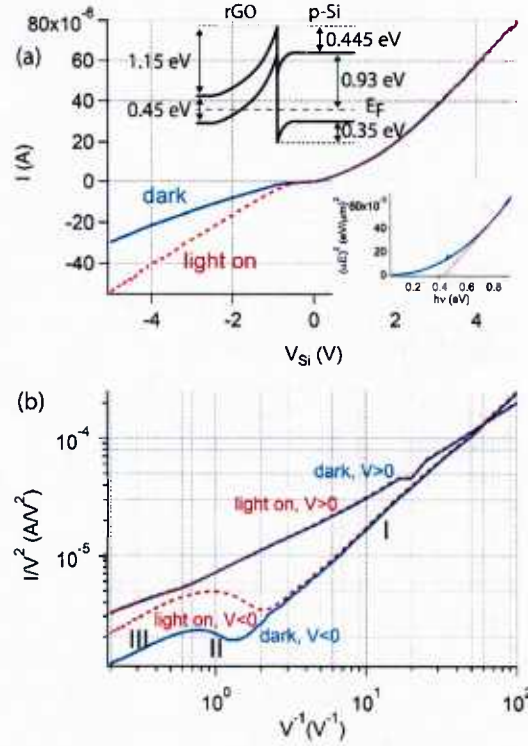


FIGURE 2. (a) Current-voltage characteristic and (b) DT plot under dark and illuminated conditions. Insets show the device energy band diagram and the rGO Tauc plot. The film thickness was 20 nm.

To further investigate the transport mechanisms we use a field-emission plot of the room temperature I-V characteristic (Figure 2(b)), which reveals a sharp change occurring near 1V in the dark reverse I-V and near 2V in the illuminated reverse I-V. At low voltages (i.e. large $1/V$ values, marked I in Figure 2(b)), the constant positive slope of the curve suggests a regime of direct tunneling transport, which will be further clarified once we reconstruct the energy band diagram of the device in what follows. Direct tunneling is well described in the context of the Simmons model,²⁰ in which tunneling across a trapezoidal barrier is considered. Under low bias, this model predicts a slope of +1 in the field emission plot,²¹ which is very near the slope obtained on the reverse currents at low bias in Figure 2(b). As the reverse voltage is increased a brief section of negative slope is observed near 1V (marked II in Figure 2(b)). The negative constant slope in this region is consistent with field-emission.²¹ In this regime, high bias (as compared with the tunneling barrier height) changes the effective tunneling barrier into a triangular shape. Further increase in the reverse voltage leads to another region of positive slope (marked II-broken gap in Figure 2(b)). Here, the most likely regime corresponds to over-the-barrier activation with series resistance in the contacts. Such

a scenario would lead to quasi-Ohmic transport,²² which also has a positive constant slope in the field emission plot (i.e. $I = GV \Rightarrow \log\left(\frac{I}{V^2}\right) = \log(G) + \log\left(\frac{1}{V}\right)$, where G is the conductance). As seen in Figure 2(b), illumination shifts the onset of field-emission emission toward lower voltages. This is consistent with over-the-barrier activation, as photons and phonons (due potentially to increase in sample temperature resulting from illumination) may help to activate electrons over the tunneling barrier.

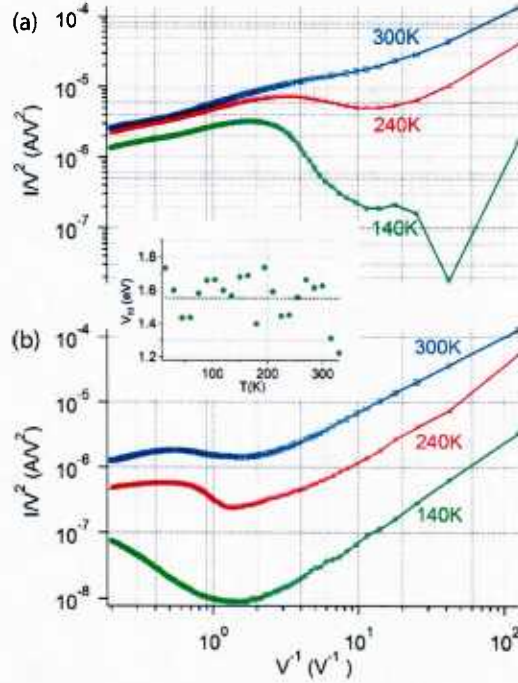


FIGURE 3. Field emission plots of the (a) forward and (b) reverse parts of the I-V characteristic. The inset shows the built-in voltage as a function of temperature.

To deduce the device band structure diagram, we measured the optical absorption of the rGO film and made a Tauc plot, as shown in the inset of Figure 2 (a). The optical band-gap of the rGO film was found to be ~ 0.45 eV. The built in potential (V_{bi}) of the rGO-Si contact was estimated by measuring I-V curves at various temperatures from 20K to 340K and performing linear fits to the high current forward portion of the curves, where conduction is limited by series resistance. V_{bi} was taken to correspond to the voltage-axis intercepts of these linear fits. We found $V_{bi} \sim 1.55$ V to be relatively uniform as a function of temperature (inset of Figure 3), indicating Fermi level pinning at surface states. A sharp decrease in V_{bi} was observed above 300K, and possibly corresponds to oxygen-impurity desorption/migration in the rGO, which has activation energy slightly above room temperature for rGO.¹⁵ Oxygen has the effect p-doping rGO,²³ thus increasing the rGO work function (which appears to be less than that of Si, see below) and shifting it closer

to that of Si. The properties of Si were extracted from the literature²² as well as the data sheet for our wafers. We found, namely, 4.05 eV for the electron affinity, 1.12 eV for the band gap, $1.12 \times 10^{16} \text{ cm}^{-3}$ for the acceptor concentration (N_a), $2.7 \times 10^{19} \text{ cm}^{-3}$ for the effective density of states in the valence band (N_v), and $9.7 \times 10^9 \text{ cm}^{-3}$ for the intrinsic carrier concentration (N_i). For the work function we have $= 4.05 + 1.12 - kT \text{ Log}(N_v/N_a) \sim 5 \text{ eV}$, where the logarithmic term corresponds to the energy difference between the Fermi level and the valence band ($\sim 0.19 \text{ eV}$). The built in voltage on the Si side (far from heterointerface) was therefore $kT \text{ Log}(N_a/N_i) = 0.35 \text{ eV}$. From this data we were able to deduce the parameters for rGO as follows, the rGO band gap was taken to correspond to the optical band gap, i.e. 0.45 eV as already discussed. Using the fact that V_{bi} corresponds to the difference in work functions between the two materials, we have $5 - 1.5 = 3.5 \text{ eV}$ for the work function of rGO. For the electron affinity, we assumed that the rGO Fermi level lies at the center of the band-gap to obtain $3.5 - 0.45/2 = 3.275 \text{ eV}$. While this assumption may not necessarily hold due to oxygen adsorbates inducing p-type doping in the rGO film, as will be seen below, the assumption affects the final proposed band diagram only marginally. For the built in voltage on the rGO side, we simply subtract the built in voltage on the Si side from V_{bi} to obtain $1.5 - 0.35 = 1.15 \text{ eV}$.

The resulting band-structure diagram is shown in the inset of Figure 2(a). It suggests that forward conduction is primarily due to holes from the p-Si to the rGO, i.e. with positive bias applied on the silicon side. Photoresponses in the reverse direction appear consistent with the mechanism of electron (i.e. minority carriers in the Si) activation over the 0.445 eV barrier. The presence of barriers in both directions helps to explain the changes in conduction mechanism noted above. In the reverse direction, low voltage, electrons in the Si see a relatively wide tunneling barrier. At mid reverse voltages, as the rGO Fermi level is pulled lower, the reverse direction barrier passes through a triangular phase leading to the negative slope in the reverse current field emission plot (Figure 2(b)). The over-the-barrier activation regime is achieved as the voltage is further increased, at which point (quasi-) Ohmic processes begin to dominate the transport. We note that the situation is similar in the forward direction, where conduction is primarily due to holes from the Si to the rGO contact. Here too, at low voltages a tunneling barrier is present and, as the positive bias on the Si is increased, its Fermi level lowers and over-the-barrier activation eventually sets in. Measurements of the temperature dependence of the I-V characteristic (Figure 3 (b)) shows that the effects of the forward direction barrier are also seen in the forward portion of the I-V characteristic, but (unlike the case for reverse conduction) only becomes prominent at low temperatures, in agreement with the smaller size of the forward direction barrier. This result also supports the proposed band energy diagram structure, and suggest that mid infrared photoresponses may also occur at low temperature under forward bias, although we did not test this possibility. The temperature dependence of the reverse current (Figure 3(b)) shows that temperature considerably enhanced the reverse voltage in the device, which is also consistent with thermal activation over the reverse conduction barrier.

II.4 – Conclusion

Our analysis suggests that the contact between rGO and p-Si leads to the formation of a type-II (broken-gap) heterojunction, with tunneling barriers in both the forward and reverse directions. This heterojunction configuration arises due to an apparently low work function of rGO and may be critical for enabling these devices to exhibit mid-infrared photoresponses at room temperature and under high reverse bias. Such parameters as the work function of rGO are heavily dependent on the preparation method and the types and concentration of oxygen-based adsorbates remaining after the reduction procedure.¹⁵ With better understanding of the relevant material parameters, the heterojunction properties could in principle be tailored so as to optimize uncooled photovoltaic sensing in different regions on the infrared spectrum. We note also that the proposed heterojunction structure also leads to the formation of a surface polarization density due to charge buildup on both sides of the heterointerface (holes in the rGO side and electrons in the Si side). Such an arrangement could also provide a mechanism for uncooled infrared sensing via photo-induced displacement currents. One reason that leads us to believe that they did not play a significant role in our devices is that the photoresponses measured did have a significant DC component.

II.5 - References

- ¹ A. Hunt, D. A. Dikin, E. Z. Kurmaev, Y. H. Lee, N. V. Luan, G. S. Chang, and A. Moewes, *Carbon* **66**, 539 (2014); A. Mathkar, D. Tozier, P. Cox, P. J. Ong, C. Galande, K. Balakrishnan, A. L. M. Reddy, and P. M. Ajayan, *J Phys Chem Lett* **3** (8), 986 (2012); Y. Shen, S. B. Yang, P. Zhou, Q. Q. Sun, P. F. Wang, L. Wan, J. Li, L. Y. Chen, X. B. Wang, S. J. Ding, and D. W. Zhang, *Carbon* **62**, 157 (2013).
- ² G. E. Fernandes, Z. Liu, J. H. Kim, C. H. Hsu, M. B. Tzolov, and J. Xu, *Nanotechnology* **21** (46) (2010); G. E. Fernandes, M. B. Tzolov, J. H. Kim, Z. J. Liu, and J. Xu, *J Phys Chem C* **114** (51), 22703 (2010).
- ³ P. L. Ong, W. B. Euler, and I. A. Levitsky, *Appl Phys Lett* **96** (3) (2010); M. B. Tzolov, T. F. Kuo, D. A. Straus, A. J. Yin, and J. Xu, *J Phys Chem C* **111** (15), 5800 (2007).
- ⁴ X. M. Wang, Z. Z. Cheng, K. Xu, H. K. Tsang, and J. B. Xu, *Nat Photonics* **7** (11), 888 (2013).
- ⁵ X. T. Gan, R. J. Shiue, Y. D. Gao, I. Meric, T. F. Heinz, K. Shepard, J. Hone, S. Assefa, and D. Englund, *Nat Photonics* **7** (11), 883 (2013).
- ⁶ A. Pospischil, M. Humer, M. M. Furchi, D. Bachmann, R. Guider, T. Fromherz, and T. Mueller, *Nat Photonics* **7** (11), 892 (2013).
- ⁷ M. Freitag, T. Low, W. J. Zhu, H. G. Yan, F. N. Xia, and P. Avouris, *Nat Commun* **4** (2013).

- 8 C. H. Liu, Y. C. Chang, T. B. Norris, and Z. H. Zhong, *Nat Nanotechnol* **9** (4), 273 (2014);
Y. Z. Zhang, T. Liu, B. Meng, X. H. Li, G. Z. Liang, X. N. Hu, and Q. J. Wang, *Nat Commun* **4** (2013).
- 9 H. X. Chang, Z. H. Sun, M. Saito, Q. H. Yuan, H. Zhang, J. H. Li, Z. C. Wang, T. Fujita, F. Ding,
Z. J. Zheng, F. Yan, H. K. Wu, M. W. Chen, and Y. Ikuhara, *Acs Nano* **7** (7), 6310 (2013).
- 10 M. Acik, G. Lee, C. Mattevi, M. Chhowalla, K. Cho, and Y. J. Chabal, *Nat Mater* **9** (10), 840
(2010).
- 11 J. T. Robinson, S. M. Tabakman, Y. Y. Liang, H. L. Wang, H. S. Casalongue, D. Vinh, and H. J.
Dai, *J Am Chem Soc* **133** (17), 6825 (2011).
- 12 B. Chitara, L. S. Panchakarla, S. B. Krupanidhi, and C. N. R. Rao, *Adv Mater* **23** (45), 5339 (2011);
F. A. Chowdhury, T. Mochida, J. Otsuki, and M. S. Alam, *Chem Phys Lett* **593**, 198
(2014); S. Ghosh, B. K. Sarker, A. Chunder, L. Zhai, and S. I. Khondaker, *Appl Phys Lett* **96** (16)
(2010).
- 13 M. Zhu, X. M. Li, Y. B. Guo, X. Li, P. Z. Sun, X. B. Zang, K. L. Wang, M. L. Zhong, D. H. Wu,
and H. W. Zhu, *Nanoscale* **6** (9), 4909 (2014).
- 14 S. Darbari, V. Ahmadi, P. Afzali, Y. Abdi, and M. Feda, *J Nanopart Res* **16** (12) (2014).
- 15 H. Seo, S. Ahn, J. Kim, Y. A. Lee, K. H. Chung, and K. J. Jeon, *Sci Rep-Uk* **4** (2014).
- 16 X. S. Wu, M. Sprinkle, X. B. Li, F. Ming, C. Berger, and W. A. de Heer, *Phys Rev Lett* **101** (2)
(2008).
- 17 R. C. de Guzman, J. H. Yang, M. Ming-Cheng, S. O. Salley, and K. Y. S. Ng, *J Mater Sci* **48** (14),
4823 (2013).
- 18 Z. P. Huang, P. Zhong, C. F. Wang, X. X. Zhang, and C. Zhang, *Acs Appl Mater Inter* **5** (6), 1961
(2013).
- 19 Jacques I. Pankove, *Optical processes in semiconductors*. (Prentice-Hall, Englewood Cliffs, N.J.,,
1971), pp.xvii.
- 20 John G. Simmons, *J Appl Phys* **34** (6), 1793 (1963).
- 21 J. M. Beebe, B. Kim, J. W. Gadzuk, C. D. Frisbie, and J. G. Kushmerick, *Phys Rev Lett* **97** (2)
(2006).
- 22 S. M. Sze, *Semiconductor devices, physics and technology*, 2nd ed. (Wiley, New York, 2002),
pp.viii.
- 23 H. E. Romero, N. Shen, P. Joshi, H. R. Gutierrez, S. A. Tadigadapa, J. O. Sofo, and P. C. Eklund,
Acs Nano **2** (10), 2037 (2008).

III - Molecular weight effects on the phase-change-enhanced temperature coefficient of resistance in carbon nanotube/ Poly(N-isopropylacrylamide) composites

**This section has been peer-reviewed for publication in IOP Nanotechnology and is awaiting final decision by the journal*

III.1 – Introduction

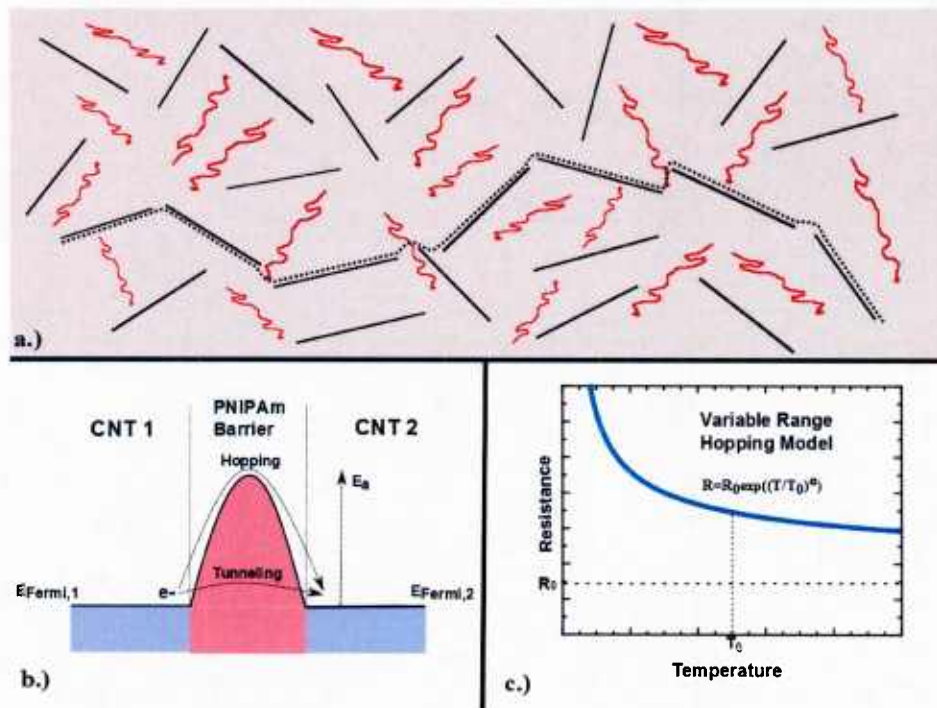


FIGURE 1. a) Illustration of network of CNTs (straight lines) and polymers (wavy lines). The dotted line represents the main conduction path. b.) Simplified band diagram showing hopping and tunneling through the PNIPAm barrier. c.) Theoretical plot of resistance over temperature for the VRH model.

Carbon nanotubes (CNTs) have received much attention due to their promising electrical, mechanical, and optical properties¹. CNT-based composites have achieved new benchmarks in terms of strength, light-weight, and durability, and offer the promise of smart materials that can sense and react to external stimuli and to changes in the environment². One particularly interesting application is in thermal imaging detectors³⁻⁷. In these sensors, the temperature coefficient of resistance (TCR) is an important figure of merit because the detector's responsivity is directly proportional to the TCR⁸. Charge transport

in carbon nanotube composites with an insulating matrix, such as a polymer, is effected via tunneling and hopping of electrons across CNT contacts⁹. This mechanism dictates that even small temperature-induced changes in the matrix dielectric properties can effect large changes in the resistance of the composite, and thus lead to high TCR. (Figure 1.a, illustrating the network of the conduction path; Figure 1.b illustrating the tunneling and hopping across CNT contacts) Recently, we reported on a CNT composite with the phase-change polymer poly-n-isopropylacrylamide (PNIPAm) that experienced large changes in the permittivity and volume as a function of humidity and temperature. PNIPAm is a thermosensitive polymer that undergoes a hydrophilicity phase transition at a lower critical solution temperature (LCST) of $\sim 32\text{ }^{\circ}\text{C}$ ¹⁰. When moisture is present, the transition is accompanied by a volume-phase transition (VPT), in which the polymer absorbs (or expels) moisture and grows (or shrinks) in volume¹¹. These changes were shown to result in large TCR ($\sim -10\%/K$) near and below PNIPAm's LCST and a similar enhancement in the responsivity to infrared light under operation as a bolometric sensor¹². In this work, we conducted an investigation into the mechanism of charge transport underlying the large TCR observed in these composites by varying the PNIPAm molecular weight, the temperature and humidity over large ranges. Better engineering of these composites and other molecular weights have enabled us to achieve even larger TCR, ($\sim -60\%/K$) than previously. We show that charge transport is consistent with the variable range hopping (VRH) model¹³ with an exponent of $1/4$, indicating transport in a 3D system¹⁴. (Figure 1.c, illustrating the VRH). Stable VRH regimes (i.e. constant activation energy) are achieved both before and after the VPT, but a pronounced change in the activation energy occurs between these regimes as a result of the VPT. Moreover, the hopping activation energy and the TCR are found to increase with the molecular weight of PNIPAm. We attribute this behavior to the degree of folding/stretching of PNIPAm chains of various lengths in response to change in temperature and humidity. The exceptionally high TCR and its dependence on humidity and molecular weight are attractive for thermal and humidity sensing applications.

III.2 – Experiment

The CNT composite films contained single-walled carbon nanotubes (SWCNT) of mixed chirality and with mean length of 1 micron. They were made via filtration of 1 mL of 1 mg/L SWCNT solution (Nanointegris Inc.) through a 20 nm pore anodized aluminum oxide (AAO) membrane filter to form a thin Bucky-paper. Then 100 μL (10 mg/mL solution in chloroform) of the insulating phase transition polymer PNIPAm (Polymer Source, Inc.) was applied atop the CNT film. PNIPAm of various molecular weights were used, namely 2.5K, 5.5K, 21.5K, and 560K, with polydispersities of 1.15, 1.18, 1.45, and 3.0, respectively. The relatively small polydispersity values indicate that measured differences between different samples are indeed due to the variation of polymer molecular weights. The film was

then dried in air, and resulted in a final weight ratio of 1:1000 between CNTs and PNIPAm. The variation of this weight ratio between different samples was found to be insignificant based on the experimental results. Devices were prepared by attaching a rectangular piece cut from the AAO membrane filter onto a glass substrate. Contacts were made with silver paste to the extremities of each rectangular piece. The wires were anchored to the glass substrates with epoxy to relieve tension and prevent damage to the contacts. Resistance measurements were made in a two-probe geometry, as four point probe measurements previously done on these composites indicated that contact resistances are negligible. Two types of experiments were conducted. First the resistance was measured as the temperature was varied (above and below the dew point) in a chamber with constant relative humidity (RH). The relative humidity was maintained by a controller which supplied dry air (from a commercial air dryer) or wet air (by passing dry air through a water bubbler). It is worth noting that the dew point is a function of the air temperature, humidity, and the sample surface temperature, thus can shift by a few degrees with the air temperature. The second set of experiments involved measuring the composite's resistance under high vacuum from 50 K to 250 K, making it possible to extract model parameters for the system over a large range of temperatures and in the absence of water.

III.3 – Results and Discussion

Figure 2 shows the temperature dependence of the resistance for samples of CNT composites with different PNIPAm molecular weights (MW) measured in vacuum. The temperature behavior of the resistance is consistent with the VRH model. In VRH, the DC conductivity is given by

$$\sigma = \sigma_0 \exp \left(- \left(\frac{T_0}{T} \right)^\alpha \right) \quad (1)$$

where T_0 is a parameter that depends on the tunneling barrier height and width, along with the dielectric constant of the material. T_0 corresponds to the hopping activation energy, i.e. $E_a = kT_0$, where k is the Boltzmann constant.

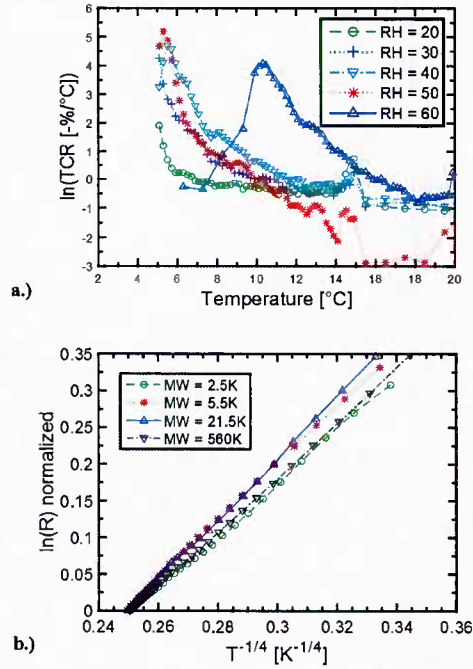


FIGURE 2. a) Temperature behavior of the TCR of a sample composite with PNIPAm MW = 560K at different relative humidities. b.) The log of the resistance in vacuum is linear with $T^{-1/4}$. This allows $T_{o,vac}$ to be calculated via the slope, $T_{o,vac} = m^4$.

The data were plotted in the form of $\ln R$ vs. $T^{-1/4}$ (according to equation 1), allowing $E_{a,vac}$, the value of E_a in vacuum, to be extracted from the slopes. This reveals the typical activation energy of barriers formed by the polymer between different CNTs in the composite when there is no atmospheric influence from compounds such as O_2 and H_2O . $E_{a,vac}$ is of great interest because it describes the nature of the typical “pristine” barrier between CNTs. It was found to vary with the molecular weight of PNIPAm (13 to 25 meV). This barrier activation energy is consistent with previously reported values from studies of similar types of CNT-polymer composite systems^{15,16}.

Over the temperature range of the polymer’s phase transition (VPT) in the composites, the TCR, defined as the percent change in the resistance per unit temperature, were measured with the samples in contact with a partial humidity atmosphere. In the case of the samples with PNIPAm MW = 21.5K and 560K, a TCR as high as -60% was obtained (table 1). It should be noted that while these two samples achieved a similar maximum TCR, the MW = 560K sample displayed enhanced TCR over a larger temperature range, meaning that its resistance changed by a greater amount during the VPT. This ultrahigh TCR value could lead to significant advances in infrared, thermal, and humidity sensing applications. However, in this report we will keep our focus on the TCR’s dependence on molecular

weight and the underlying conduction mechanism. The optical/infrared response is not characterized here as these measurements were done in a previous study of this material system¹².

TABLE I. Parameters of linear fits at different molecular weights (MW) leading to the extracted values of $E_{a,vac}$. Also included are the maximum observed values of TCR and the $E_a/E_{a,vac}$ ratio for a relative humidity of 60%.

MW	Linear Fit R^2	T_0 (K)	$E_{a,vac}$ (meV)	R_0 (k Ω)	Max $E_a/E_{a,vac}$	Max TCR (%/ $^{\circ}$ C)
2.5K	0.9984	160.6	13.8	74.5	3.6	-14.7
5.5K	0.9995	236.1	20.4	127.2	5.9	-20.2
21.5K	0.9993	288.1	24.8	110.2	9.0	-60.2
560K	0.9997	183.4	15.8	216.9	20	-59.4

The dynamics of the experiment under a humid atmosphere are much more complex than those performed in vacuum. In a humid atmosphere, the polymer can freely interact with water molecules present in the surrounding air, and at sufficiently low temperatures water vapor can condense onto the sample and provide a “limitless” water supply, thus greatly affecting the TCR. The degree to which moisture can interact with the system varies greatly with the sample temperature (relative to the LCST) as well as the availability of moisture. When the sample is cooled below the LCST in an environment with at least some available moisture, the PNIPAm polymer chain admits water into its structure and unfolds, leading to the VPT. The VPT occurs as newly available water molecules move along the polymer chain and alter its conformation, causing the polymer chains to occupy a greater volume. The degree to which to polymer folding and conformation is affected by the availability of water is expected to depend to some extent on the size of the chain this provides the motivation for performing the experiment reported here in which the PNIPAm of various molecular weights are tested. The resulting increase in volume leads to an increase in the tunneling barrier width between the CNTs. Additionally, the VPT has been shown to significantly alter the relative dielectric permittivity of PNIPAm, from ~ 17 (below 32C) to ~ 63 (above 32C)¹⁷. This increase in the dielectric constant, due to the large dielectric constant of the water entering the structure, corresponds to an increase in the barrier height, which ultimately leads to an increase in the barrier activation energy¹⁸. Both of these effects (volume and dielectric permittivity increase) cause a substantial growth in barrier activation energy, creating a dramatic increase in the composite resistance at the onset of the VPT.

At high temperatures (i.e. well above the LCST), the composite is in its hydrophobic state and contains only residual amounts of moisture. In this state E_a is approximately the same as $E_{a,vac}$, save for potential interaction of the CNTs with oxygen, which adsorb onto the CNT surface and “dope” the CNT

with holes¹⁹. Comparison of the sample resistances in dry air and in vacuum revealed that the effects of such oxygen doping were negligible. This made it possible to solve for R_0 using resistances measured while the temperature was still well above the dew point, R_{dry} and T_{dry} .

$$R_0 = R_{dry} \exp \left(- \left(\frac{E_{a,vac}}{k_b T_{dry}} \right)^\alpha \right) \quad (2)$$

With this we determined T_0 , (i.e. E_a) as a function of temperature

$$T_0(T) = T \left(\ln R - \ln R_{dry} + \left(\frac{E_{a,vac}}{k_b T_{dry}} \right)^\alpha \right)^{\frac{1}{\alpha}} \quad (3)$$

While R_0 could have been extracted from the linearization of the vacuum data, it was more convenient for us to get it from the data well above the dew point in the humid environment measurement. This is due to a small amount of hysteresis in the resistance of some samples at the start of each temperature sweep during the experiments. More specifically, the change in the baseline resistance at the beginning of each sweep was -0.4%, -13.6%, -2.6%, and +37.1% for samples with PNIPAm MW corresponding to 2.5K, 5.5K, 21.5K, and 560K. The likely cause of this hysteresis is that a small amount of residual water in the sample from previous sweeps, despite the annealing that was done prior to each data collection run. The process of adsorption and evaporation of water could alter the position and form of the polymer chains, which could lead to positive or negative changes in resistance. The large amount of positive hysteresis displayed by the 560K sample could indicate that it retained substantially more water than the other samples after each sweep as a result of its much greater chain length. As will be further explained below, this water would cause an increase in sample resistance. Extracting R_0 from this experiment normalizes out these hysteretic differences and makes it easier to illustrate how the barrier activation energy changes during the VPT.

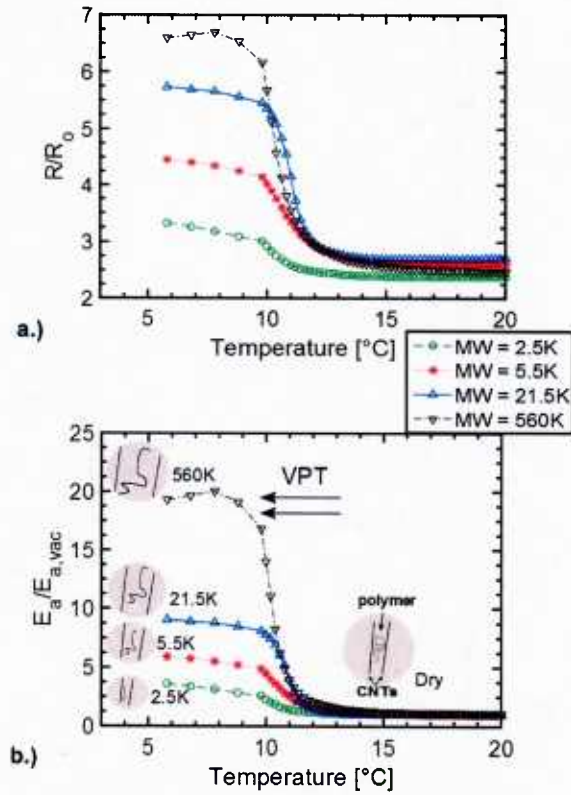


FIGURE. 3. a) Temperature behavior resistance with different PNIPAm MW at RH = 60%. b.) The growth ratio of E_a relative to $E_{a,vac}$ over temperature. Illustrations show spacing between CNTs increasing with molecular weight after the VPT.

The temperature behavior of resistance in a humid environment is characterized by a sharp increase in resistance shortly after the dew point. The barrier activation energy, E_a , exhibits similar behavior, increasing greatly below the dew point (figure 3). The magnitude of increase in E_a relative to $E_{a,vac}$ reflects the manner in which the hopping barrier changes during hydration. This change also depends on the molecular weight of the PNIPAm because the process of moisture uptake depends on the size of the polymer chain. The fitting parameters and other system properties for the different samples are shown in table 1. The value of E_a remains relatively constant after the VPT takes place (i.e. at low temperatures), indicating that a regime of stable VRH is achieved shortly after the transition.

E_a experiences higher growth during hydration for large MW. We attribute this to smaller polymer chains being able to more effectively alter their conformation and less hindered by the CNT dispersed in them during the VPT and thus occupy the space surrounding the CNTs in a more compact manner. Their relatively smaller size gives them less need to displace CNTs relative to each other, which

overall results in comparatively smaller changes in the tunneling barriers. On the other hand, the larger molecular chains have significantly more tendency to displace nearby CNTs in order to complete their conformation change.

When the PNIPAm is not hydrated, it occupies significantly less volume and its folding must be taken into account. An interesting feature of our data is that $E_{a,vac}$ for the MW = 560K sample was actually significantly smaller (15.8 meV) than that of the next smaller MW = 21.5K sample (24.8 meV). This is a reversal of the expected trend of larger E_a for larger MW. One potential reason is related to the dynamics of polymer chain collapse during the VPT which has been found to depend on the MW²⁰. We note that the MW = 560K sample is 20-fold larger than the other samples studied, and possibly underwent a significantly larger degree of chain collapse/expansion during the VPT. Most of the polymer mass is concentrated inside the collapsed structure rather than being uniformly distributed to create barriers between CNTs. This agrees with the measurements reported in Plunkett et al.²⁰, which show a marked onset of chain collapse for MW between 60K and 230K. The lower $E_{a,vac}$ for the MW = 560K sample and its enhanced collapse/expansion also contributes the very large E_a enhancement observed during the VPT.

III.4 – Conclusion

Films of CNTs homogenously dispersed with PNIPAm polymers of different molecular weights were prepared and studied, resulting in TCR as large as -60 %/°C across the dew point. The large TCR is a result of VRH electron transport across the polymer between CNT contacts, with a characteristic temperature exponent of $\frac{1}{4}$. Temperature and humidity both control the changes in the hopping activation energy. Larger polymer molecular weights were observed to further enhance the TCR effect via more substantial collapse/expansion of the polymer chain structure across the VPT. With such phase-change-enabled effects, one important challenge consists in broadening the range of temperatures across which the high TCR ensues. For this particular class of polymers, PNIPAm, this entails finding mechanisms for engineering VPTs in more complex polymer structures or in multi-polymer compositions, as well as further studies on the mechanisms whereby water molecule interacts with the sample. For this, further efforts in both material and device engineering must be undertaken.

III.5 – Supplementary Information

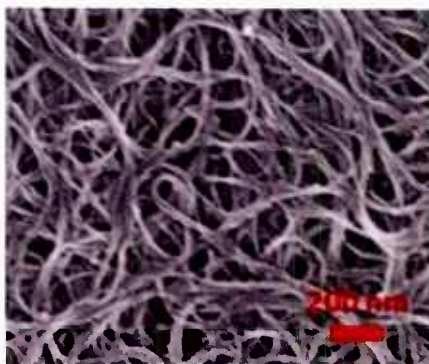


FIGURE. 4. SEM image of a sample CNT-PNIPAm composite. CNT bundles can be seen, which illustrates the random and uniform nature of their dispersion in the composite.

III.6 – References

- ¹a) M. S. Dresselhaus, G. Dresselhaus, P. Avouris, *Carbon Nanotubes: Synthesis, Structure, Properties, and Applications*, Springer, Berlin, New York **2001**; b) N. Sinha, J. Z. Ma, J. T. W. Yeow, *J. Nanosci. Nanotechnol.* **2006**, 6, 573.
- ²I. Kang, Y. Y. Heung, J. H. Kim, J. W. Lee, R. Gollapudi, S. Subramaniam, S. Narasimhadevara, D. Hurd, G. R. Kirikera, V. Shanov, M. J. Schulz, D. Shi, J. Boerio, S. Mall, M. Ruggles-Wren, *Comp. Part B: Eng.* **2006**, 37, 382.
- ³a) R. C. Jones, *J. Opt. Soc. Am.* **1953**, 43, 1; b) P. L. Richards, *J. Appl. Phys.* **1994**, 76, 1.
- ⁴a) A. E. Aliev, *Infrared Phys. Technol.* **2008**, 5, 541; b) R. T. Lu, Z. Z. Li, G. W. Xu, J. Z. Wu, *Appl. Phys. Lett.* **2009**, 94, 163110.
- ⁵M. E. Itkis, F. Borondics, A. P. Yu, R. C. Haddon, *Science* **2006**, 312, 413.
- ⁶P. Merel, J. B. A. Kpetsu, C. Koechlin, S. Maine, R. Haidar, J. L. Pelouard, A. Sarkissian, M. I. Ionescu, X. L. Sun, P. Laou, S. Paradis, *Comptes Rend. Phys* **2010**, 11, 375.
- ⁷M. Tarasov, J. Svensson, L. Kuzmin, E. E. B. Campbell, *Appl. Phys. Lett.* **2007**, 90, 163503.
- ⁸A. Y. Glamazda, V. A. Karachevtsev, W. B. Euler, I. A. Levitsky, *Adv. Funct. Mater.* **2012**, 22, 2177.
- ⁹G. C. Psarras, *Comp. Part A: Appl. Sci. and Manuf.*, **2006**, 37, 1545.
- ¹⁰M. Heskins, J. E. Guillet, *J. Macromol. Sci., Chem.* **1968**, A2, 1441.
- ¹¹H. G. Schild, *Prog. Polym. Sci.* **1992**, 17, 163.
- ¹²G. E. Fernandes, J. H. Kim, A. K. Sood, J. Xu, *Adv. Funct. Mater.* **2013**, 23, 4678.
- ¹³D. H. Zhang, K. Ryu, X. L. Liu, E. Polikarpov, J. Ly, M. E. Thompson, C. W. Zhou, *Nano Lett.* **2006**, 6, 1880.
- ¹⁴N. F. Mott, *Conduction in Non-Crystalline Materials*, Clarendon Press, New York 1987.

- ¹⁵L. Vincent, P. Romain, A. Robert, A. Laurent, A.Z Ahmed, J.L. Bantignies, *Carbon*, **2012**, 50 (14), 4987-4994.
- ¹⁶M. Abu-Abdeen, A.S. Ayesb, A.A.A. Jaafari, *J. Polym. Res.* **2012**, 19, 9839.
- ¹⁷K. Iwai, Y. Matsumura, S. Uchiyama, A.P. de Silva, *J. of Mater. Chem.* **2005**, 15, 2796.
- ¹⁸J.G. Simmons, *J. of Appl. Phys.* **1963**, 34, 1973.
- ¹⁹D. Kang, N. Park, J. Ko, E. Bae, W. Park, *Nanotechnology*, **2005**, 16, 1048.
- ²⁰K. N. Plunkett, X. Zhu, J. S. Moore, D. E. Leckband, *Langmuir*, **2006**, 22 (9), 4259.

Bibliography

- 1) Gustavo E. Fernandes, Jin Ho Kim, Matthew Chin, Nibir Dhar, and Jimmy Xu, “Carbon nanotube microbolometers on suspended silicon nitride via vertical fabrication procedure,” *Appl. Phys. Lett.* 104, 201115 (2014).
- 2) Patrick Tae, Chong Zhao, Gustavo E. Fernandes, Jin Ho Kim, and Jimmy Xu, “Molecular weight effects on the phase-change-enhanced temperature coefficient of resistance in carbon nanotube/ Poly(N-isopropylacrylamide) composites,” *IOP Nanotechnology* – awaiting final editorial decision.
- 3) Gustavo E. Fernandes, Jin Ho Kim, Declan Oller, and Jimmy Xu, “Reduced Graphene Oxide Mid-Infrared Photodetector at 300K,” manuscript under preparation.